Effect of low Zn content on corrosion resistance and biocompatibility of biodegradable Mg-Zn-Y-Zr alloys

Xinyi Zhou[1),*], *Jun Cheng*[2),*], *Jun Xu*[3)], *Yipei Mao*[1)], *Yang Dong*[1)], *Yixuan He*[4)], *and Meifeng He*[1),✉]

1) School of Materials Science and Engineering, University of Shanghai for Science and Technology, Shanghai, 200093, China
2) Northwest Institute for Nonferrous Metal Research, Shaanxi Key Laboratory of Biomedical Metal Materials, Xi'an 710016, China
3) Department of Gastrointestinal Surgery, Changhai Hospital of Shanghai, Shanghai 200433, China
4) State Key Laboratory of Solidification Processing, Northwestern Polytechnical University, Xi'an, 710072, China
* These authors contributed equally to this paper.
✉Corresponding author: Meifeng He E-mail: hmf752@usst.edu.cn

Abstract

Although the degradability and biosafety of magnesium alloys make them advantageous for biological applications, medical implants made of magnesium alloys often fail prematurely due to corrosion. Therefore, improving the corrosion resistance of magnesium alloys has become an urgent problem in the alloy design process.

In this study, we designed and prepared Mg-xZn-0.5Y-0.5Zr (x = 1, 2, and 3 wt%) alloys in a hot extruded state and analyzed their surface structure through scanning electron microscopy (SEM), energy dispersion spectrometry (EDS), and X-ray diffraction (XRD). It was found that increasing the Zn content refined the recrystallized grains in the alloy. Particularly in Mg-3Zn-0.5Y-0.5Zr, the I phase became finer, forming both granular and nanoscale needle-like particles. Surface characterization after the immersion experiment showed that the corrosion product layer was mainly composed of $Mg(OH)_2$, $Mg(OH)_2$, $Zn(OH)_2$, $CaCO_3$, and hydroxyapatite. The corrosion rate of the alloy was measured using hydrogen evolution and weight loss methods. The degradation rate of ZW305K was the lowest, at about 4.1 and 6.0 mm/year. Electrochemical experiments further explained the corrosion circuit model of the alloy in solution and confirmed the earlier results. The maximum polarization resistance of ZW305K was 375.83Ω, and the lowest corrosion current density was 0.104 mA/cm2. As a biomedical alloy, it must exhibit good biocompatibility, so the alloy was also tested through cytotoxicity, cell adhesion, and staining experiments. The cell viability of each group after 48 h was greater than 100%, showing that the addition of zinc enhances the alloy's biocompatibility. In

summary, the prepared alloys have the potential to be used as biodegradable implant materials.

1. Introduction

Magnesium (Mg) and its alloys have the advantages of low densities, high specific strengths, paramagnetism, degradability, and biocompatibility, and they have broad application prospects as biomedical degradable materials [1-3]. However, Mg and its alloys are chemically very active, corroding easily and degrading rapidly in the physiological environment of the body, which hinders their further development in the medical field [4]. Therefore, improving the corrosion resistance of medical degradable Mg alloys is of great significance for their clinical applications.

Some researchers have found that surface modification, composition design, and structural optimization of magnesium alloys can reduce their biodegradation rate [5-8]. The corrosion resistance of magnesium alloys can be improved through several methods. The first method involves adding some alloying elements such as Zn and Zr at the beginning of the alloy design, which can easily improve the corrosion resistance of the alloy [9-12]. The second method is to reduce the equilibrium potential of magnesium matrix by plastic deformation. The third method involves adding a corrosion-resistant coating to the surface of the magnesium alloy [13-14]. By applying an organic or inorganic coating, a bone-implant interface is formed on the surface [15]. The fourth method is heat treatment, which reduces micro-galvanic corrosion in the alloy, increases the self-corrosion potential of the matrix, and improves the corrosion resistance of the alloy [16].

The design of suitable Mg alloy compositions is considered to be a straightforward and cost-effective way to add appropriate alloying elements to Mg alloys[17]. According to previous studies, the addition of elemental Zn to Mg alloys improves the strength and ductility while being beneficial to the human body[11], and low concentrations of elemental Zn can increase the matrix potential [18-21]. The rare earth element Zr is a "purifying element" that not only purifies the alloys of Fe, Cu, and other impurity elements but also refines the grain size and improves the corrosion resistance of the alloy [22]. The addition of Y can also affect the corrosion properties and strengths of the alloys [23-25]. In recent years, the Mg-Zn-Y series of alloys have been widely studied by researchers due to their good corrosion resistance, biocompatibility, and mechanical properties. Jin et al. [26] reported a class of Mg-Zn-Zr-Nd/Y alloys with good strength and ductility, which were found to have good cytocompatibility and osteoblasticity in cellular experiments. Li et al.[27] then found that the Mg-2Y-1Zn-0.4Zr alloy showed enhanced cytocompatibility after heat treatment and extrusion and exhibited the best degradation properties, and the alloy is expected to be a new biodegradable implant material.

The equilibrium potential of the Mg matrix is reduced by plastic deformation to

refine the dynamic recrystallization grains and make the distribution of solute atoms more uniform [28]. Abundant grain boundaries provide nucleation sites for the passivation film, forming a dense surface protection layer. The resistance imbalance of the alloy is reduced, preventing the formation of a microgalvanic cell and improving corrosion resistance [29].

Although a great deal of research has been conducted on Mg-Zn-Y-Zr alloys, there are few reports on the effect of low Zn contents on the corrosion resistance and biocompatibility of Mg-Zn-Y-Zr alloys in the extruded state. Therefore, in this paper, Mg-xZn-0.5Y-0.5Zr (x = 1, 2, 3 wt%) alloys were prepared using a hot extrusion method; the effects of low Zn contents on the microstructures, corrosion resistance, and biocompatibility of the alloys were investigated.

2. Materials and methods

2.1 Preparation of Mg-Zn-Y-Zr alloys

The Mg-Zn-Y-Zr alloys were prepared from high-purity Mg (99.9 wt.%), zinc (99.9 wt.%), the Mg-30Zr intermediate alloy, and the Mg-30Y intermediate alloy. The actual compositions of the samples were determined by inductively coupled plasma optical emission spectroscopy (ICP-OES, Varian 700), and the measured compositions of the alloys are shown in Table 1.

The alloy was melted using a pit-type resistance furnace and a high-temperature-resistant crucible. Pure Mg was preheated and placed in the crucible for melting, while a mixture of $CO_2 + SF_6$ was introduced as a protective gas. After the pure Mg was melted, the temperature was raised to 850°C, and the intermediate alloys were added. Then, the furnace temperature was raised to 900°C and held for 10 min with stirring. After 5 min of standing, the molten liquid was poured into a preheated high-temperature-resistant mold and cooled to room temperature under a high-purity Ar atmosphere to obtain ingots with diameters of 60 mm. These ingots were subsequently subjected to solution treatment at 480°C for 10 h. Finally, the ingots were extruded into 12 mm bars at a temperature of 320°C with an extrusion ratio of 25:1.

The Mg-xZn-0.5Y-0.5Zr alloy was labeled as the ZWx05K alloy. In this labeling, "Z" denotes the element Zn, "W" denotes the element Y, "x" denotes the nominal mass fraction of Zn, "05" denotes the nominal mass fraction of Y, and "K" denotes the solid solution element Zr.

Table 1. Compositions of Mg-Zn-Y-Zr alloys

Identification code	Sample	Actual composition (wt.%)				
		Zn	Y	Zr	Fe	Mg

ZW105K	Mg-Zn-0.5Y-0.5Zr	0.83	0.42	0.54	0.0080	Bal.
ZW205K	Mg-2Zn-0.5Y-0.5Zr	1.56	0.49	0.56	0.0085	Bal.
ZW305K	Mg-3Zn-0.5Y-0.5Zr	2.80	0.32	0.65	0.0081	Bal.

2.2 Microstructure characterization

The samples were sanded with SiC sandpaper and polished. A mixture of 6 g of picric acid, 10 ml of acetic acid, 10 ml of water, and 70 ml of ethanol was chosen as the etching agent [30], and etching was performed for 5 s for subsequent microstructural observation. The microstructures were observed with an optical microscope and a scanning electron microscope (SEM, Sigma 300), and the phase structures of the alloys were analyzed to determine the chemical compositions based on energy-dispersive X-ray spectroscopy (EDS, Oxford Xplore 30), which was performed with accelerating voltages ranging from 0.02 to 30 kV, continuously adjustable in 10 V steps. The alloy samples were studied by X-ray diffraction (XRD, D8 Advance) using Cu-Kα radiation in the scanning range of 15°–85° with a scanning step of $4° \cdot min^{-1}$.

2.3 In-vitro corrosion resistance

1) Electrochemical testing

Electrochemical tests were performed on the samples in simulated body fluid (SBF, pH = 7.4) at 37°C. The samples were used as the working electrode and the reference electrode. A three-electrode system was selected, in which the sample was the working electrode, the area to be tested was 1 cm², and a platinum sheet and saturated calomel electrode were used as the counter electrode and reference electrode, respectively.

2) Hydrogen precipitation and weight loss experiments

Calculations of the hydrogen precipitation and weight loss were performed through immersion experiments. The chosen experimental setup is shown in Fig. 1, which consisted of an inverted burette and funnel [31]. The specimens were machined into small pieces with dimensions of Ø10 mm × 5 mm and then weighed and immersed in an aqueous SBF solution at 37°C for 168 h. The average corrosion rate (CR, mm·year⁻¹) can be calculated using the following equation:

$$CR = \frac{8.76 \times 10^4 \times (W_1 - W_0)}{A \times t \times \rho} \tag{1}$$

where W_0 is the original mass of the sample (g), W_1 is the mass of corrosion products removed from the surface of the sample (g), A is the area exposed by the

sample (cm^2), t is the immersion time (h), and ρ is the density of the sample (g/cm^3).
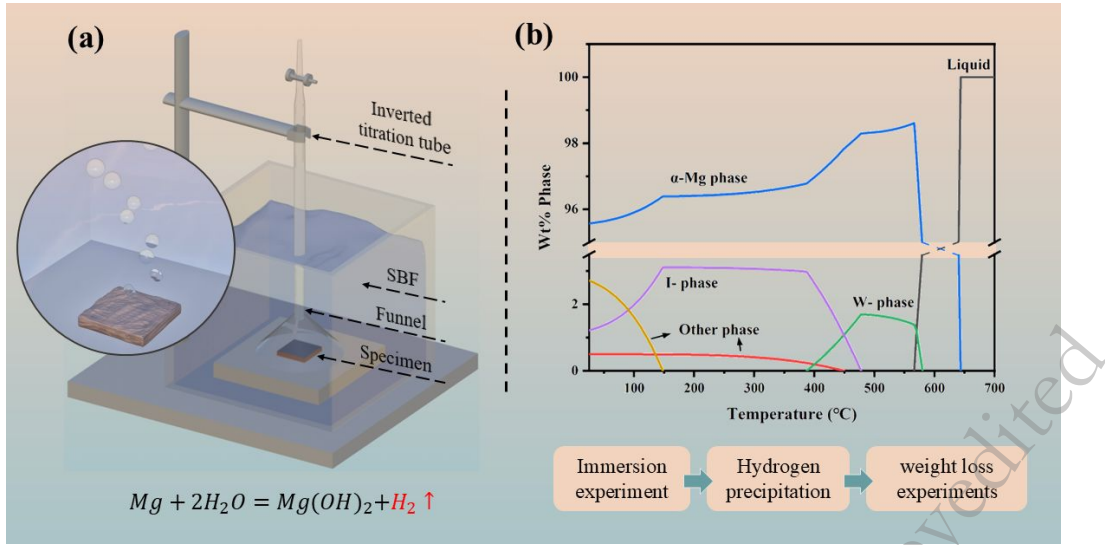

Fig. 1. (a) Schematic diagram of hydrogen analysis experimental device (b) Prediction and simulation of the precipitated phase

2.4 Biocompatibility tests

Mouse embryonic osteoblasts (MC3T3-E1) (purchased from Shanghai Shenrui Biotechnology Co., Ltd.) were added into α-minimal essential medium (MEM) containing 10% fetal bovine serum (FBS) and were cultured in a cell culture incubator at 37°C with 5% CO_2.

The leach solution of the alloy was prepared according to ISO 10993 Part 12 [32]. Under cell culture conditions, the alloy samples were immersed in α-MEM medium containing 10% FBS. The leachate was diluted by a factor of nine according to the recommendation of Wang et al. [33] for subsequent cell experiments. All experiments were performed in triplicate.

1) Cell viability

The Cell Counting Kit-8 (CCK-8) method was used to assess the cell viability. First, 110 μl of MC3T3-E1 cell suspension with a cell density of 2×10^4 /ml was taken and inoculated into 24-well plates. After 24 h of incubation, the original medium was replaced with 500 μl of extracts of different alloys, and fresh cell culture medium was set up as a control group. The supernatant was removed after 24, 48, and 72 h of incubation, and a mixture of α-MEM medium containing 10% CCK-8 was added. The incubation was continued for 4 h before the optical density (OD) value at 450 nm was measured in each well by an automated enzyme labeling instrument. The relative growth rate (RGR) was calculated as follows:

$$RGR = \frac{OD_{test}}{OD_{control}} \times 100\% \tag{2}$$

where OD_{test} is the average OD value of the experimental group, and $OD_{control}$ is the average OD value of the control group.

2) Cell adhesion and spreading

The three alloy samples were placed in 24-well plates, and 500 μl of cell suspension with a cell density of 2×10^5/ml was added to each well. After 4 and 24 h of incubation, the plates were rinsed three times with phosphate buffer solution (PBS) and fixed with 2.5% (w/v) glutaraldehyde solution for 4 h. Finally, the plates were rinsed again with PBS solution, after which they were gradually dehydrated with alcohols at concentrations of 35%, 45%, 75%, 90%, and 100% and then were sprayed with gold. The cells were observed to adhere to the samples using SEM.

3) Alkaline phosphatase activity staining

Alkaline phosphatase (ALP) staining can be used to assess the osteogenic properties of alloys [34]. An MC3T3-E1 cell suspension with a cell density of 1×10^4 ml^{-1} was inoculated into six-well plates and cultured for 24 h. After 24 h, the medium was replaced with either the extract of the alloys or α-MEM medium (control). After the cells were cultured for 3 and 7 d, they were treated following the procedure outlined in the 5-bromo-4-chloro-3-indolyl phosphate (BCIP)/nitro blue tetrazolium (NBT) Instruction Manual and were finally photographed with a digital camera. The effect of the extracts on the alkaline phosphatase activity could be assessed by observing the dark and light areas of the colors.

2.5 Data analysis

All data used in this study were tested for statistical differences using one-way analysis of variance (ANOVA) followed by Bonferroni post hoc tests. Statistical differences were measured at $*p < 0.05$, $**p < 0.01$, and $***p < 0.001$.

3. Results and discussion

3.1 Phase analysis and microstructure
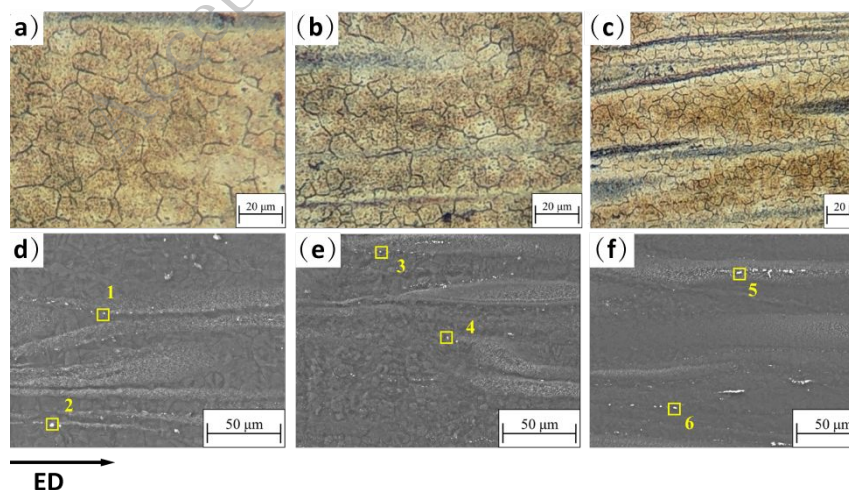

Fig. 2. (a – c) Optical microstructure of ZW105K alloy, ZW205K alloy, and ZW305K

alloy; (d－f) Scanning electron microscopy (SEM) images of the microstructures of the ZW105K, ZW205K, and ZW305K alloys.

Fig. 2(a), (b), and (c) shows the optical microstructures of the ZW105K, ZW205K, and ZW305K alloys, respectively. Due to the occurrence of the dynamic recrystallization (DRX) during the extrusion deformation process, the grain size became non-uniform, and the grain sizes of the ZW105K, ZW205K, and ZW305K alloys were 12.91 ± 0.88 μm, 11.54 ± 0.72 μm, and 8.13 ± 0.53 μm, respectively, with a gradual decrease in the grain sizes. This indicates that the increase in the Zn content in the range of 1–3% could refine the grain size to a certain extent. The microstructure of the alloy is shown in Fig. 3. Refined α-Mg grains appeared in the DRX zone, the grains in this region became finer, and the number of grain boundaries in the alloy increased. However, in the non-dynamically recrystallized zone, the grains wrapped around the crushed second phase solidified within the alloy and were distributed along the extrusion direction to form a striped and non-uniformly distributed grouping.

According to a previous report [35], the types of second phases in these alloys vary based on the mass ratio of Zn to Y. When Zn/Y is 1.5–2, the second phase is α-Mg + W-phase ($Mg_3Zn_3Y_2$); when Zn/Y is 2–2.5, it is the α-Mg + W-phase + I-phase (Mg_3Zn_6Y); and when Zn/Y is 5–7, it is the α-Mg + I-phase. The composition of the second phase in each alloy was analyzed according to these guidelines. The points in Fig. 2(d–e) were analyzed with EDS; the results are shown in Fig. 3(a). The particles in the alloys were mainly composed of Mg, Zn, and Y. In the ZW105K and ZW205K alloys, the atomic number ratios of Zn and Y in the second phase were close to 3:2, with Mg accounting for a high mass fraction. Thus, it can be hypothesized that the composition of the second phase was α-Mg and the W-phase. In the ZW305K alloy, the value of Zn/Y at point 6 was approximately equal to 6, indicating the presence of the I-phase in the second phase of the ZW305K alloy. To further determine the phase composition, the alloy samples were analyzed with XRD, as shown in Fig. 3(b). The results confirmed that the physical phase of the alloy consisted mainly of α-Mg, the W-phase ($Mg_3Zn_3Y_2$), and the I-phase (Mg_3Zn_6Y), depending on the Zn content. The number of diffraction peaks of the W-phase increased when the Zn content was above 2%, indicating that more W-phases formed in the ZW205K alloy. When the zinc content increased to 3%, a new weak I-phase diffraction peak appeared in the ZW305K alloy. Because the contents of the W- and I-phases in the alloy were much lower than that of α-Mg, the corresponding characteristic peaks were not evident.
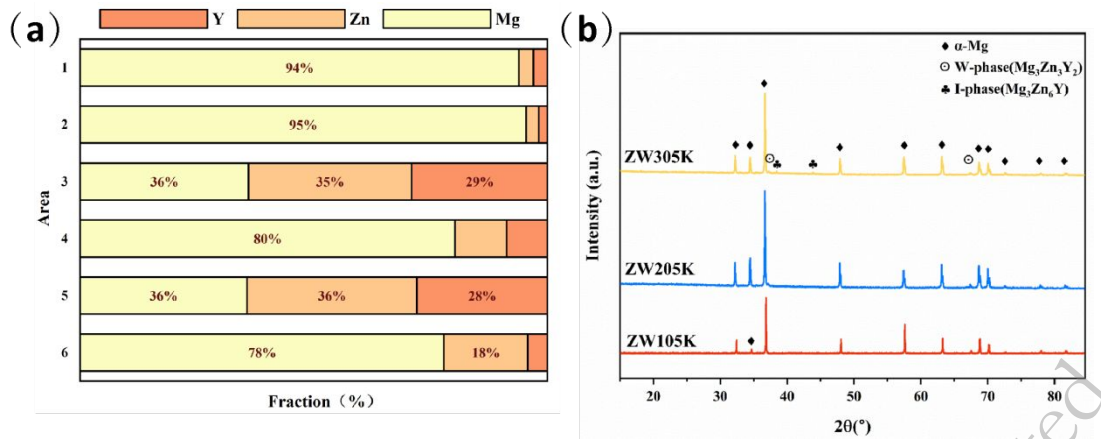
Fig. 3. (a) EDS results at points in Fig. 2 and (b) X-ray diffraction (XRD) patterns of the ZW105K, ZW205K, and ZW305K alloys.

3.2 In-vitro corrosion resistance

Fig. 4 shows the polarization curves of different samples in the SBF solution. Based on the polarization curves and the Butler–Volmer equation [36], the corrosion potential (Ecorr), corrosion current density (icorr), and Tafel slopes (βa and βc) at the anode and cathode were determined, and the collated data are shown in Table 2. It can be seen that the addition of Zn increased the corrosion potential (Ecorr) from −1.72 to −1.67 V, and the corrosion current density (icorr) decreased from 1.25×10^{-3} to 1.04×10^{-4} A·cm^{-2}. The values of corrosion current density, which to some extent reflects the corrosion resistance of the samples [37-38], showed that the ZW305K alloy sample had the lowest icorr.
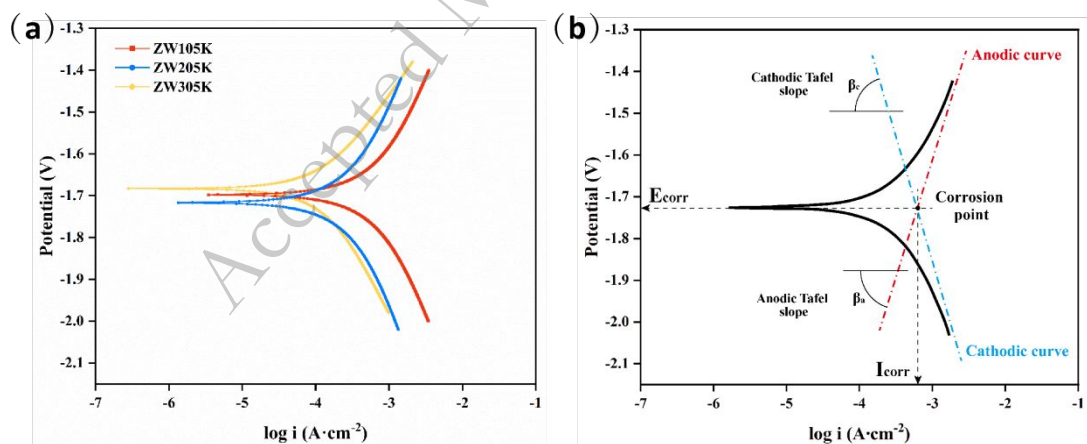

Fig. 4. (a) Polarization curves of the ZW105K, ZW205K, and ZW305K alloys, and (b) example diagram of polarization curves

Table 2. Record of polarization curve parameters

8

Samples	Ecorr (V)	Icorr (A·cm^{-2})	βa (mV·dec^{-1})	βc (mV·dec^{-1})
ZW105K	−1.70	1.25×10^{-3}	743.2	619.6
ZW205K	−1.72	3.09×10^{-4}	396.1	451.2
ZW305K	−1.67	1.04×10^{-4}	152.9	224.5

The AC impedance spectra respond to the microscopic mechanism of material corrosion in a corrosive media [39]. Fig. 5 shows typical electrochemical impedance plots of the specimens, and Table 3 shows the associated data. Fig. 5(a) shows the Nyquist plots as well as the equivalent circuit diagram of the prepared materials. In general, the larger the radius of the capacitance ring is, the higher the corrosion resistance in the solution is [40]. The ZW305K alloy exhibited the largest radius of the capacitance ring. In the equivalent circuit diagram, Rs is the solution resistance, Rct is the charge transfer resistance, Rf is the corrosion product layer resistance, and the constant phase elements CPEdl and CPEdf represent the double layer capacitances at the interface of the alloy and solution and the capacitance effect caused by the corrosion product layer, respectively. Furthermore, the inductance L1 was used to simulate the low-frequency inductive loop, which was a characteristic of the occurrence of pitting corrosion in the specimen. It can be seen that the Rct of ZW305K was the highest, reaching 264.3 Ω, while the Rf values were in the order of ZW105K < ZW205K < ZW305K, which indicated that the film layer of the alloy matrix became thicker with the increase in the Zn content. The densification was also improved, and it was difficult for the corrosive medium to penetrate deeper into the matrix. The Bode phase angle and impedance diagrams are shown in Fig. 5(b) and (c). The ZW305K alloy had the largest peak, which implied that it had the best corrosion resistance. In the extruded alloy group, the plastic deformation effectively refined the grains, and the solute atoms were evenly distributed through dynamic recrystallization. Abundant grain boundaries can provide nucleation sites for the passivation film, thereby forming a dense surface protection layer. At the same time, the potential imbalance is reduced, which can reduce the formation of micro-galvanic cells [41], resulting in better corrosion resistance.
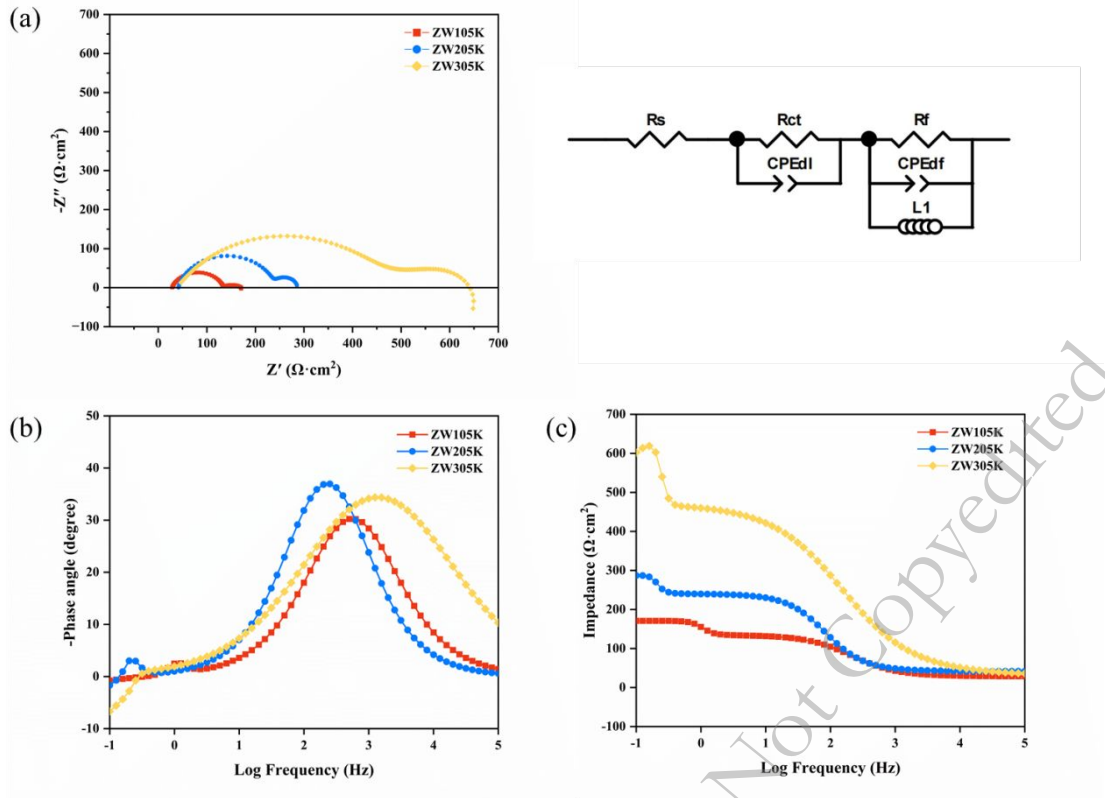
Fig. 5. Alternating current (AC) impedance diagrams of ZW105K, ZW205K, and ZW305K: (a) Nyquist vs. equivalent circuit, (b) Bode diagram—phase angle vs. frequency, and (c) Bode diagram—impedance vs. frequency

Table 3 AC impedance spectrum fitting data

Sample	R_s ($\Omega \cdot cm^{-2}$)	R_{ct} ($\Omega \cdot cm^{-2}$)	CPE_{dl}		R_f ($\Omega \cdot cm^{-2}$)	CPE_{df}		L_1 (H)
			Y_1 ($S \cdot cm^{-2} \cdot s^{-n}$)	n_1		Y_2 ($S \cdot cm^{-2} \cdot s^{-n}$)	n_2	
ZW105K	41.33	199.3	22.2	0.865	48.67	5600	0.905	345
ZW205K	32.265	137.5	644	0.897	135.1	4069	2.695	35.59
ZW305K	40.52	264.3	34.4	1.676	610.2	1699	0.519	5115

Fig. 6(d), (e), and (f) shows the amount of hydrogen precipitated, weight loss, and pH changes, respectively, during the corrosion process for the three alloys immersed in SBF for 168 h. The amount of hydrogen precipitated from each alloy in the SBF increased with the increase in the immersion time, and the results showed the following order: ZW105K > ZW205K > ZW305K. In general, the corrosion rate decreased with the increase in the Zn content. Generally, the corrosion mechanism of the Mg alloy in aqueous solutions can be described by the following reaction equations [42]:

$$Mg + 2H_2O \rightarrow Mg(OH)_2 + H_2\uparrow, \qquad (3)$$

Anodic reaction:

$$Mg \rightarrow Mg^{2+} + 2e^-, \tag{4}$$
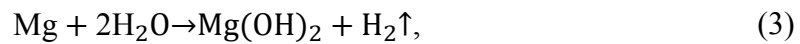
Cathodic reaction:

$$2H_2O + 2e^- \rightarrow H_2 \uparrow + 2OH^-. \tag{5}$$

The corrosion of Mg alloys in solution mainly generated Mg(OH)$_2$ accompanied by hydrogen generation, and the actual measurements of the hydrogen precipitation method were lower than those of the weight loss method because of the loss of the generated hydrogen [43-45]. The corrosion rates of the ZW305K alloy measured with the hydrogen precipitation method and weight loss method were 4.1 and 6.0 mm/year, respectively, which were the lowest degradation rates. Fig. 6(f) shows the pH change of each sample after 7 d of immersion. The change in pH was related to the production of OH$^-$ in the solution, and the lower pH showed a better resistance to degradation. After 7 d of immersion in SBF, the pH of the ZW305K was the lowest, at only approximately 8.8, which further indicated that the ZW305K alloy had the best resistance to degradation.
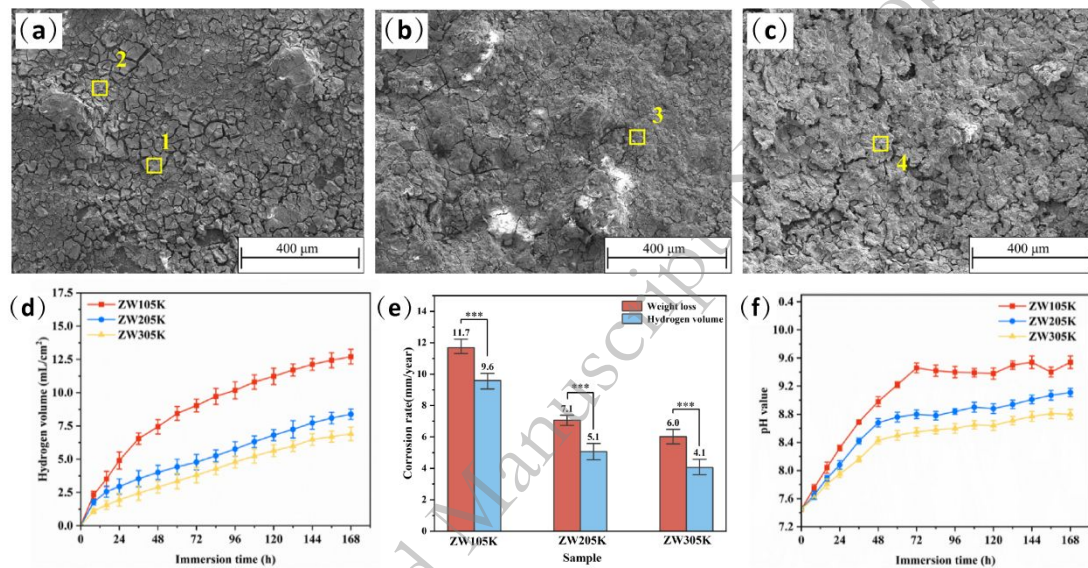

Fig. 6. Corrosion surface morphologies of (a) ZW105K, (b) ZW205K, and (c) ZW305K after 7 d of immersion in SBF; ZW105K–ZW305K characteristics over 7 d of immersion in simulated body fluid (SBF): (d) hydrogen precipitation curves, (e) corrosion rates measured by hydrogen precipitation and weight loss methods, and (f) pH change plots

The surface morphologies of the corrosion products of each alloy are shown in Fig. 6. The macroscopic surfaces of all the alloys showed varying degrees of cracked corrosion product layers, as well as irregular corrosion pits. The formation of corrosion pits originated from the further erosion caused by Cl$^-$ in the solution at the locations where the corrosion products were dislodged [46-47]. The ZW305K alloy with the highest Zn content had the densest corrosion product layer, which provided more effective protection to the substrate and had a relatively low level of corrosion. The presence of the elements O, Mg, Zn, Ca, and P on the surfaces of all three

samples was also observed, as well as some C, as shown in Fig. 8(a). The EDS results indicated that the flake products in this alloy were $Mg(OH)_2$ and a small amount of $Zn(OH)_2$, while $CaCO_3$ and hydroxyapatite (HAP) might also have been deposited on the surface [48-49]. Fig. 7 shows the cross-sectional corrosion products and the corresponding elemental distributions of the three alloy samples after immersion in SBF solution for 7 d. The elemental C content was relatively high on the corrosion surface of the alloy, indicating that the surface was rich in cations such as Mg^{2+} and Zn^{2+}, which facilitates the attraction of CO_3^{2-} from the solution. The corrosion pits of the ZW105K alloy were wide and deep, in contrast to the smaller pits of the ZW205K and ZW305K alloys.
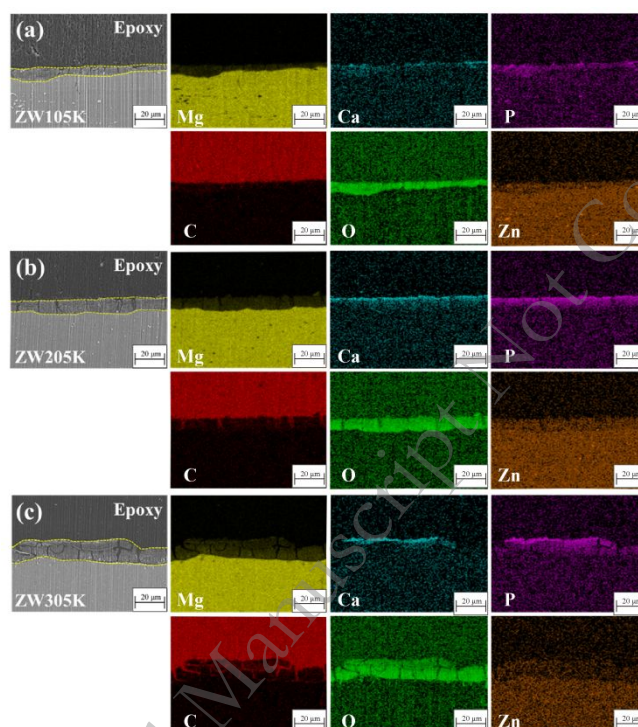

Fig. 7. Cross-sectional corrosion products and corresponding elemental distributions of the (a) ZW105K, (b) ZW205K, and (c) ZW305K alloys after 7 d of immersion in SBF
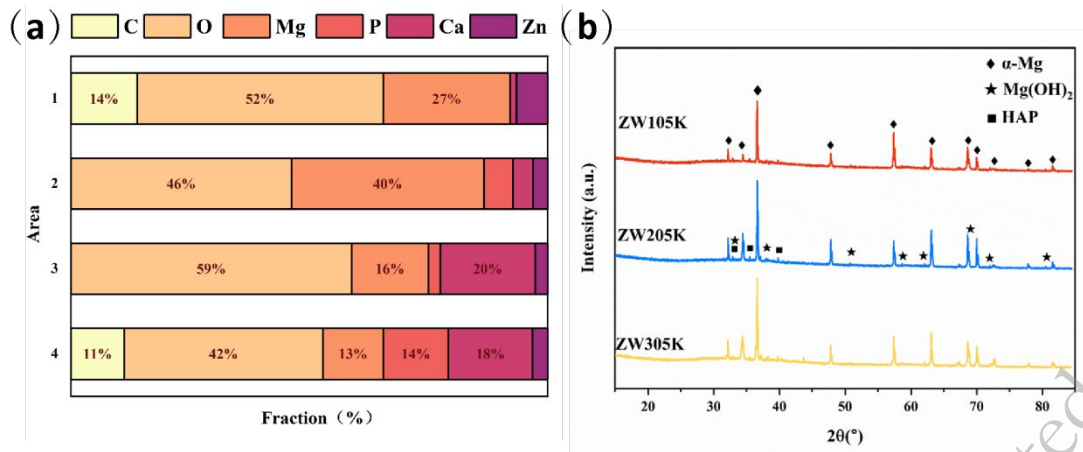
Fig. 8. (a) EDS results for points in Fig. 6; (b) XRD diffractograms of alloys with corrosion products

Based on the EDS elemental distribution diagrams, it can be seen that the corrosion product layer consisted of two parts. The outermost layer was rich in Ca, P, and a small amount of C, and the inner layer was rich in Mg, Zn, and O. To further determine the compositions of the corrosion products, the samples with the corrosion products were subjected to XRD phase analysis, as shown in Fig. 8(b). The XRD patterns indicated that the corrosion products were mainly composed of $Mg(OH)_2$ and HAP, because the corrosion products had high concentrations in the inner layer. The $Zn(OH)_2$ and $CaCO_3$ contents were low, and no corresponding peaks appeared. Previous studies [50] have shown that the presence of HAP can enhance the activity of osteoblasts, which suggests that the alloys had a certain degree of biocompatibility.
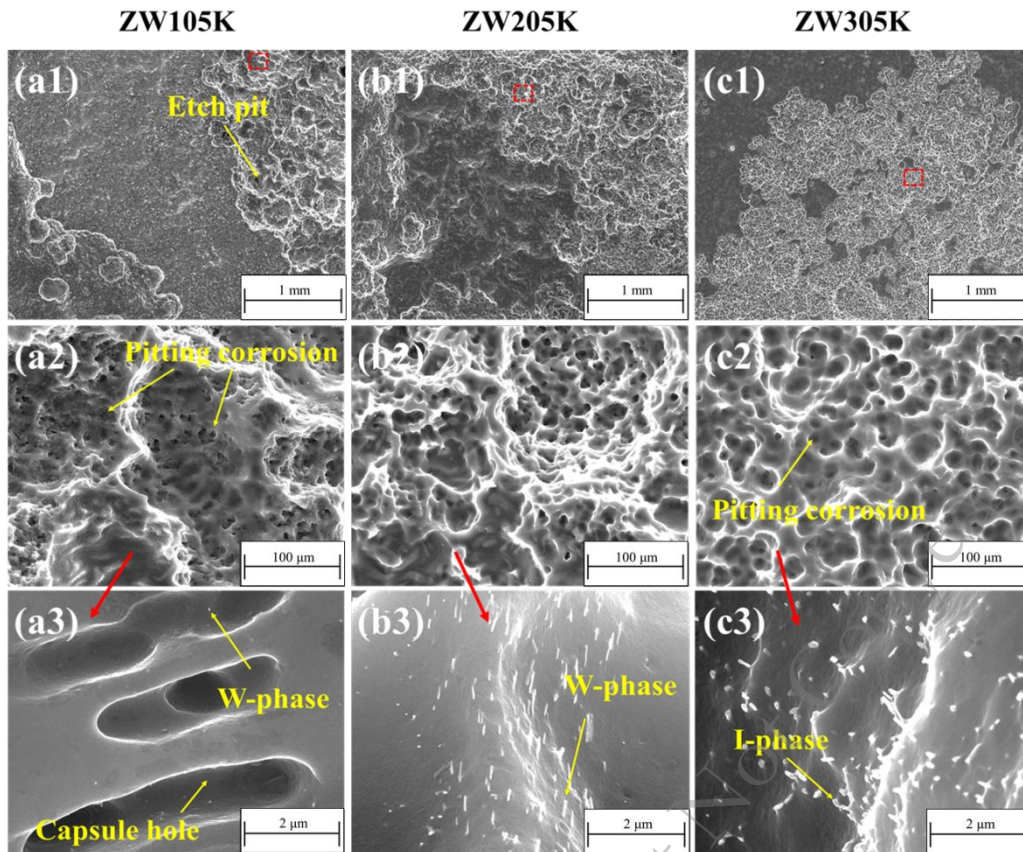
Fig. 9. (a1–a3) ZW105K, (b1–b3) ZW205K, and (c1–c3) ZW305K alloy surfaces after removal of corrosion products and their localized enlargements

Fig. 9 shows the surface topographies of the corrosion products removed from each alloy. From the magnified images of Fig. 9(a1)–(c2), it can be observed that the surfaces of each alloy showed pitting corrosion behavior, and at the lower terrain, the morphology was the typical morphology with corroded dynamically recrystallized grains [51], creating a porous appearance. The corrosion process initially started at the grain boundaries of the α-Mg matrix and further developed into unevenly sized corrosion pits, with the centers of the grains as the bottoms of the pits and the peripheries of the grain boundaries as the edges. The corrosion pits produced for the ZW105K were large and deep, suggesting that this alloy was prone to homogeneous corrosion in the SBF. In contrast, the surfaces of the ZW205K and ZW305K alloys showed less corrosion, and the corrosion pits were large and dense with smaller areas. Fig. 9(a3) shows a fine capsule pore-like appearance, which was presumed to be due to the presence of corrosion products on the surface slowing down the corrosion process in this area. Some nanoscale second phases, such as needle-like phases, are shown in Fig. 9(a3)–(b3), which were presumed to be the crushed fine W-phase and I-phase during the extrusion process.

The second phases, consisting of a ternary alloy of Mg, Zn, and Y, were significantly more noble than the α-Mg matrix, and they acted as the cathode in microcells during the corrosion process. Previous results [35] showed that the

presence of either a single I- or W-phase in the alloy enhanced the corrosion resistance of the alloy, which was worse due to the microcurrent effect between the W-phase and the α-Mg matrix. Due to the uniform distribution of the crushed W-phase on the extrusion strip and the ability of the I-phase to balance the potential [52-54], the ZW305K alloy showed the best corrosion resistance.

Combined with the results of electrochemical analysis and SEM, the microstructural changes of the alloys during the simulated corrosion of the SBF could be inferred, as shown in Fig. 10. Two kinds of grains appeared inside the alloy after extrusion and deformation: dynamically recrystallized grains and large uncrystallized grains wrapped with a broken second phase. Broken W-phases were present in all the alloys, and nano-sized needle-like and fine granular I-phases newly appeared in the ZW305K alloy. The second phase provided a corrosion barrier and microcurrent effect in the corrosion reaction. In the ZW105K, when corrosion occurred, $Mg(OH)_2$ was generated on the surfaces of the α-Mg grains. The layer was easily dissolved, and the exposed matrix continued to be degraded by corrosion. In contrast, the presence of more W-phase in the ZW205K was helpful for resisting further corrosion attack, and the formation of the thicker alternating $Mg(OH)_2$ and $Zn(OH)_2$ film layers covering the substrate on the surface provided good protection. In the ZW305K alloy, the surrounding α-Mg grains were less susceptible to corrosion because the presence of the I-phase provided a balancing potential. In addition, the increase in the Zn content made the recrystallized grains smaller and the number of grain boundaries larger, making it difficult for corrosion to proceed across the grain boundaries [55], improving the corrosion resistance of the alloy.

Apatite deposition was found in the corrosion products of the alloy and SBF, and this phenomenon was attributed to the following. After the corrosion reactions on the surface of the substrate, the surface was enriched with a large number of electronegative OH^- and PO_4^{3-} ions. Positively charged Ca^{2+} was attracted to the surface of the substrate and combined with electronegative ions to deposit on the surface of the substrate, forming hydroxyapatite, and at the same time, providing the alloy substrate with a dense protective film.
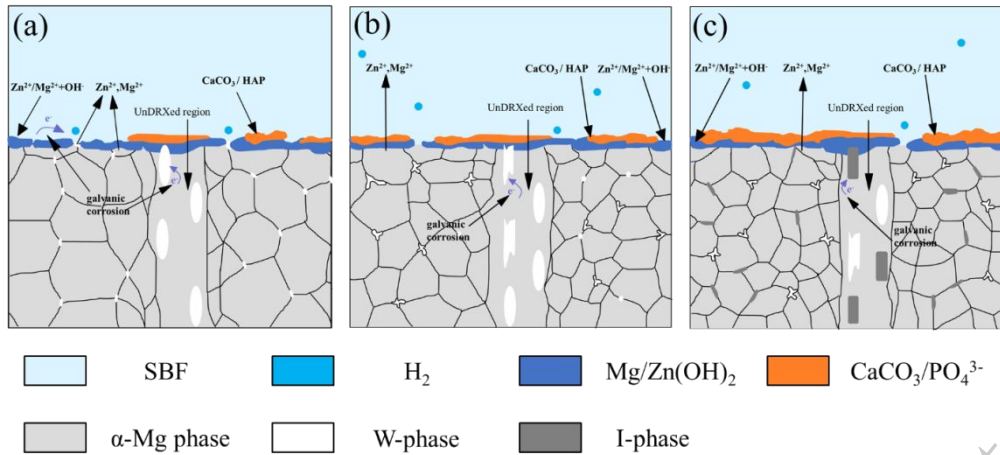
Fig. 10. Microstructural changes of (a) ZW105, (b) ZW205K and (c) ZW305K after corrosion in SBF

3.3 Biocompatibility

As shown in Fig. 11 the cell viability gradually increased with the prolongation of the culture time. After 24 h, the cell viability of each alloy group was lower than 100%, which may have been due to the release of excessive Mg^{2+} ions from the alloys in the short term, which led to osteoblast shock [56] and suppressed cell proliferation. The cell viability of each group after 48 h was greater than 100%, indicating that the osteoblasts gradually developed an Mg^{2+} tolerance. After 72 h, the cells in all the groups entered a rapid multiplication stage, which may have been due to the excellent corrosion resistance of the alloy, resulting in a weakening of the effect of the drastic release of Mg^{2+} in the short term, and also due to the presence of moderate concentrations of Mg^{2+} and Zn^{2+} in the extraction solution, which promoted osteoclast proliferation and differentiation [57]. However, it was shown that high concentrations of Zn^{2+} induced apoptosis in different cells and tissues [58]. The lowest cell viability was observed for the ZW305K alloy, which may have been due to the inhibition of cell differentiation by the high concentration of Zn^{2+} present in the extract. According to the ISO standard 10993-5 [59], for a cell viability above 75%, the material can be considered to be non-cytotoxic. Thus, it can be confirmed that the alloy had good cellular activity against MC3T3-E1 osteoblasts.
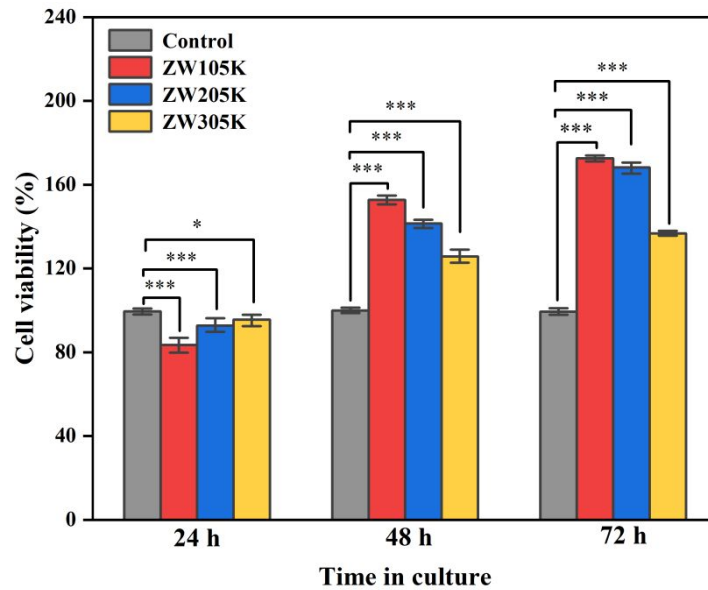
Fig. 11. Cell survival of MC3T3-E1 cells after 24, 48, and 72 h of incubation in alloy extracts

By observing the growth state of the cells, it was possible to analyze the proliferation and adhesion of the cells produced under the direct influence of the material, which may have affected the adhesion of the cells due to the generation of hydrogen gas by the contact of the Mg alloys with the aqueous environment [60]. As can be seen from Fig. 12, after 4 h of cell spreading, cells in the shape of round balls generated plate-like pseudopods and adhered to the surfaces of the alloy specimens. After 24 h, with the extension of the incubation time, the Mg alloy reacted with the products in the medium, generating pine-needle-like crystals on the surface, while the roughness and cracks on the surface of the material increased, which impeded the survival of the cells to some extent [61]. The cells, which spread out, showed flattened shapes with needle-like synapses found at the anterior ends, which were found to be well adherent. The cells could proliferate and grow better due to the lack of significant cytotoxicity of the alloy material as well as the precipitation of HAP, providing an osteoinductive layer for early cell adhesion.
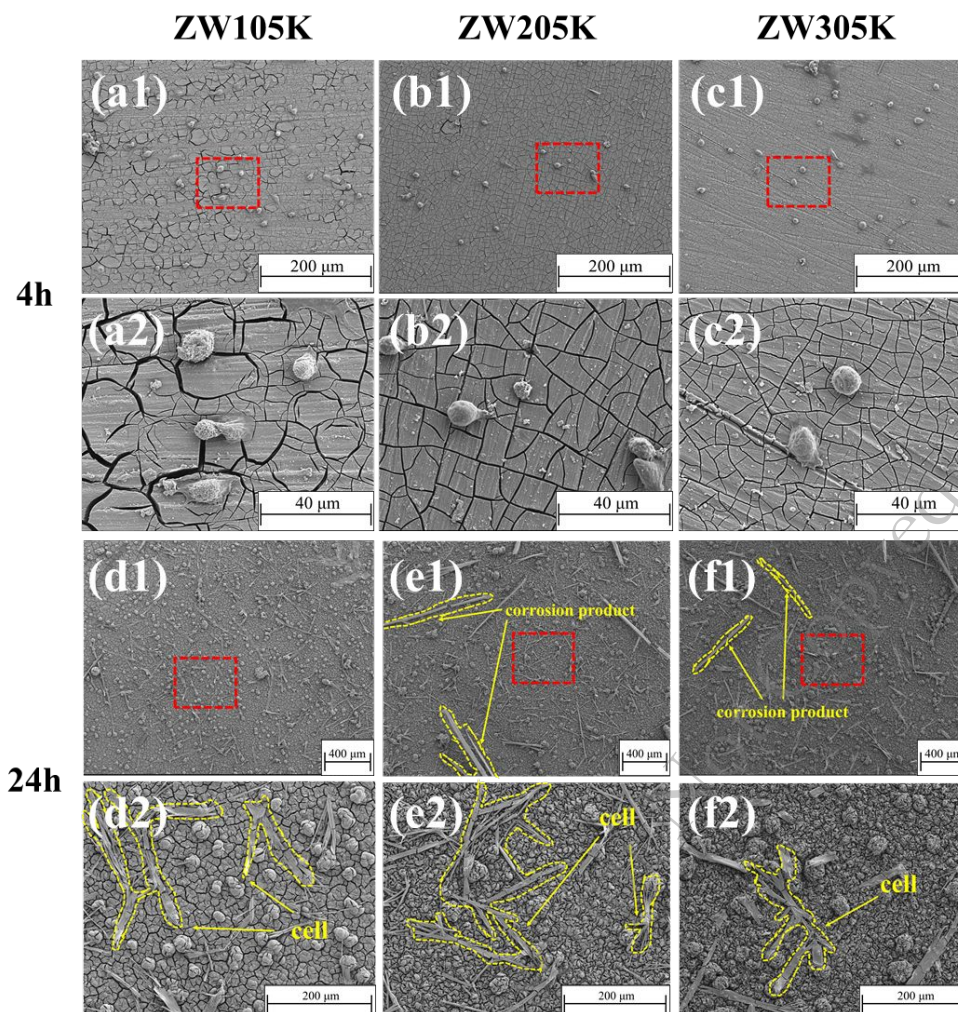
Fig. 12. Cell adhesion and morphologies on the sample surfaces after cell spreading. After 4 h: (a1) ZW105K (low magnification, LM) and (a2) ZW105K (high magnification, HM); (b1) ZW205K (LM) and (b2) ZW205K (HM); and (c1) ZW305K (LM) and (c2) ZW305K (HM). After 24 h: (d1) ZW105K (LM) and (d2) ZW105K (HM); (e1) ZW205K (LM) and (e2) ZW205K (HM); and (f1) ZW305K (LM) and (f2) ZW305K (HM).

Fig. 13 shows the results of the staining experiments of MC3T3-E1 cells after culturing, in which the blue dots are the nuclei, and the red areas are the actin of the cells [62]. After 4 h of culturing, the cells in each group were sparsely distributed. The cells, which were initially in a round ball-like shape, had not yet fully expanded, with some slower-extending cells matching the shape and size of their nuclei. After adhesion, the cells became fully extended in all directions, and some of them exhibited star and spindle morphologies, while bundled actin microfilaments were also observed, along with multiple amorphous raised pseudopods forming on the surface. The pseudopods of one cell preferred to be in contact with the pseudopods of the neighboring cells, a phenomenon that was particularly evident in ZW105K. In ZW305K, cellular actin overlap could be observed, suggesting strong cellular

anchorage.

The results of ALP staining of osteoblasts after the addition of each alloy extract to the culture are shown below the dotted line in Fig. 13. After 3 d of culturing, ALP was uniformly dispersed in the culture dish, and the color depths of the groups were almost identical. However, the color depth of the alloy group was slightly lighter than the control group, which indicated that the excessive alkaline environment in the α-MEM medium and the alloy extract inhibited the ALP hydrolysis, indicating that the alloys did not promote osteoblast activity in the short term. However, after 7 d, the ALP activities in the experiments were all higher than those of the control group, and the ZW105K group had the darkest color in the figure, which corresponded to the highest cell proliferation rate, which was consistent with the results of the cell viability assay
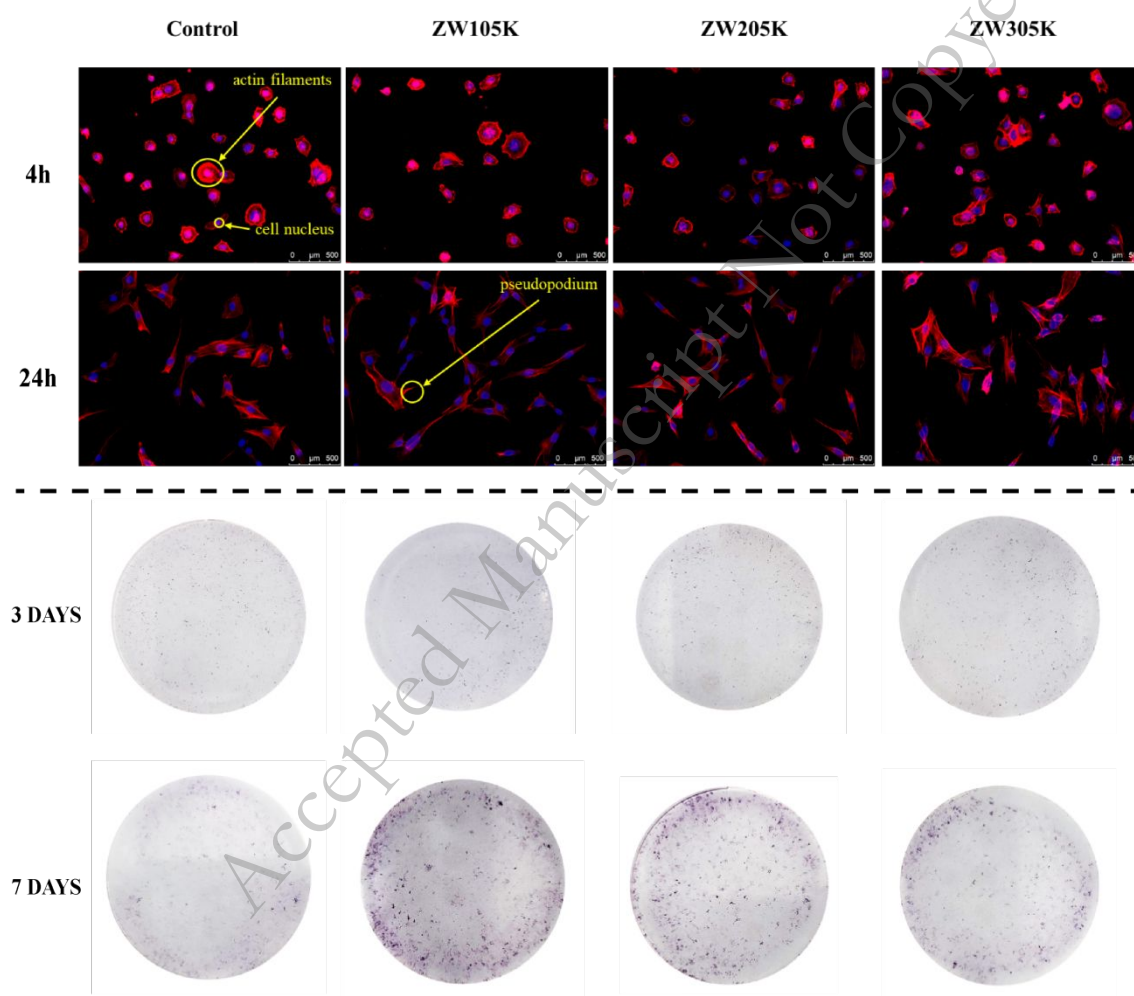

Fig. 13. Results of the phalloidin staining assay of MC3T3-E1 cells after 4 and 24 h of culturing and (below the dotted line) alkaline phosphatase (ALP) staining of MC3T3-E1 cells after 3 and 7 d of incubation in each alloy extract

4. Conclusions

This paper focused on the influence of the variation in the elemental Zn content on the corrosion resistance as well as on the biocompatibility of Mg-xZn-0.5Y-0.5Zr (ZWx05K, x = 1, 2, 3 wt%) alloys. The experimental results can be summarized as follows:

(1) The microstructure of the ZWx05K alloy is composed of α-Mg and a secondary phase. With an increase in the Zn content, the secondary phase transitions from the I phase (Mg_3Zn_6Y) to the W phase ($Mg_3Zn_3Y_2$), with a significant refinement of grains due to the addition of Zn.

(2) The extrusion process promotes the uniform distribution of the W phase in sheet-like structures along the extrusion belt. The I phase contributes to potential balancing, enabling the ZW305K alloy to achieve the shortest passivation film formation time and the best corrosion resistance.

(3) An increase in the Zn content leads to a thicker corrosion product composed of $Mg(OH)_2$, $Zn(OH)_2$, and $CaCO_3$/HAP. This dense corrosion product layer help improves the corrosion resistance of the alloy.

(4) With the increase of Zn^{2+} concentration, the cell activity decreases gradually; however, the cell activity value remains greater than 80%, indicating that the alloy exhibits no apparent cytotoxic effects on MC3T3-E1 cells.

Acknowledgments

References

[1] S. Amukarimi, and M. Mozafari, Biodegradable magnesium-based biomaterials: An overview of challenges and opportunities, *MedComm*, 2(2021), No.2, p. 123.

[2] X. Li, X.M. Liu, S.L. Wu, K.W.K. Yeung, Y.F. Zheng, and P.K. Chu, Design of magnesium alloys with controllable degradation for biomedical implants: From bulk to surface, *Acta Biomater.*, 45(2016), p. 2.

[3] D. Zhao, F. Witte, F. Lu, J. Wang, J. Li, and L. Qin, Current status on clinical applications of magnesium-based orthopaedic implants: A review from clinical translational perspective, *Biomaterials*, 112(2017), p. 287.

[4] W. Li, W. Qiao, X. Liu, D. Bian, D. Shen, Y. Zheng, J. Wu, K.Y.H. Kwan, T.M. Wong, K.M.C. Cheung, and K.W.K. Yeung, Biomimicking Bone-Implant Interface Facilitates the Bioadaption of a New Degradable Magnesium Alloy to the Bone Tissue Microenvironment, *Adv. Sci.*, 8(2021), No.23, p. 2102035.

[5] S. Lesz, B. Hrapkowicz, M. Karolus, and K. Golombek, Characteristics of the Mg-Zn-Ca-Gd Alloy after Mechanical Alloying, *Materials*, 14(2021), No.1, p. 14010226.

[6] K. Sheng, W. Li, P. Du, D. Mei, S. Zhu, L. Wang, and S. Guan, Shortening the manufacturing process of degradable magnesium alloy minitube for vascular stents by introducing cyclic extrusion compression, *J. Magnesium Alloys*, 12(2024), No.8, p. 3204.

[7] J.-l. Su, J. Teng, Z.-l. Xu, and Y. Li, Biodegradable magnesium-matrix composites: A review, *Int. J. Miner. Metall. Mater.*, 27(2020), No.6, p. 724.

[8] S. Zhang, X. Zhang, C. Zhao, J. Li, Y. Song, C. Xie, H. Tao, Y. Zhang, Y. He, Y. Jiang, and Y. Bian, Research on an Mg–Zn alloy as a degradable biomaterial, *Acta Biomater.*, 6(2010), No.2, p. 626.

[9] J.-w. Chang, J. Duo, Y.-z. Xiang, H.-y. Yang, W.-j. Ding, and Y.-h. Peng, Influence of Nd and Y additions on the corrosion behaviour of extruded Mg-Zn-Zr alloys, *Int. J. Miner. Metall. Mater.*, 18(2011), No.2, p. 203.

[10] A.V. Koltygin, V.E. Bazhenov, I.V. Plisetskaya, V.A. Bautin, A.I. Bazlov, N.Y. Tabachkova, O.O. Voropaeva, A.A. Komissarov, and V.D. Belov, Influence of Zr and Mn additions on microstructure and properties of Mg—2.5wt%Cu—Xwt%Zn (X = 2.5, 5 and 6.5) alloys, *Int. J. Miner. Metall. Mater.*, 29(2022), No.9, p. 1733.

[11] K. Wen, B.-Q. Xiong, Y.-A. Zhang, X.-W. Li, Z.-H. Li, L.-Z. Yan, H.-W. Yan, and H.-W. Liu, Aging precipitation characteristics and tensile properties of Al–Zn–Mg–Cu alloys with different additional Zn contents, *Rare Metals*, 40(2021), No.8, p. 2160.

[12] A.V. Koltygin, V.E. Bazhenov, R.S. Khasenova, A.A. Komissarov, A.I. Bazlov, and V.A. Bautin, Effects of small additions of Zn on the microstructure, mechanical properties and corrosion resistance of WE43B Mg alloys, *Int. J. Miner. Metall. Mater.*, 26(2019), No.7, p. 858.

[13] D. Wang, C. Ma, J. Liu, W. Li, W. Shang, N. Peng, and Y. Wen, Corrosion resistance and anti-soiling performance of micro-arc oxidation/graphene oxide/stearic acid superhydrophobic composite coating on magnesium alloys, *Int. J. Miner. Metall. Mater.*, 30(2023), No.6, p. 1128.

[14] J. Ma, X. Lu, S.P. Sah, Q. Chen, Y. Zhang, and F. Wang, Enhancing corrosion resistance of plasma electrolytic oxidation coatings on AM50 Mg alloy by inhibitor containing Ba(NO3)2 solutions, *Int. J. Miner. Metall. Mater.*, 31(2024),

No.9, p. 2048.

[15] D. Saran, A. Kumar, S. Bathula, D. Klaumünzer, and K.K. Sahu, Review on the phosphate-based conversion coatings of magnesium and its alloys, *Int. J. Miner. Metall. Mater.*, 29(2022), No.7, p. 1435.

[16] J. Han, C. Wang, Y. Song, Z. Liu, J. Sun, and J. Zhao, Simultaneously improving mechanical properties and corrosion resistance of as-cast AZ91 Mg alloy by ultrasonic surface rolling, *Int. J. Miner. Metall. Mater.*, 29(2022), No.8, p. 1551.

[17] Y. Liu, Y. Zheng, X.-H. Chen, J.-A. Yang, H. Pan, D. Chen, L. Wang, J. Zhang, D. Zhu, S. Wu, K.W.K. Yeung, R.-C. Zeng, Y. Han, and S. Guan, Fundamental Theory of Biodegradable Metals-Definition, Criteria, and Design, *Adv. Funct. Mater.*, 29(2019), No.18, p. 1805402.

[18] C.T. Chasapis, P.-S.A. Ntoupa, C.A. Spiliopoulou, and M.E. Stefanidou, Recent aspects of the effects of zinc on human health, *Arch. Toxicol.*, 94(2020), No.5, p. 1443.

[19] M. Liu, J. Wang, S. Zhu, Y. Zhang, Y. Sun, L. Wang, and S. Guan, Corrosion fatigue of the extruded Mg-Zn-Y-Nd alloy in simulated body fluid, *J. Magnesium Alloys*, 8(2020), No.1, p. 231.

[20] H. Li, S. Qin, Y. Ma, J. Wang, Y. Liu, and J. Zhang, Effects of Zn content on the microstructure and the mechanical and corrosion properties of as-cast low-alloyed Mg–Zn–Ca alloys, *Int. J. Miner. Metall. Mater.*, 25(2018), No.7, p. 800.

[21] W. Wang, X. Zhang, A. Zhang, H. Yu, X. Kang, C. Wang, Y. Song, J. Ni, M.L. Zheludkevich, and X. Zhang, High-performance Mg–Zn alloy achieved by the ultrafine grain and nanoparticle design, *Bioact. Mater.*, 41(2024), p. 371.

[22] Y. Chen, T. Ying, Y. Yang, J. Wang, and X. Zeng, Regulating corrosion resistance of Mg alloys via promoting precipitation with trace Zr alloying, *Corrosion Sci.*, 216(2023), p. 111106.

[23] L. Shi, Y. Yan, C.-s. Shao, K. Yu, B. Zhang, and L.-j. Chen, The influence of yttrium and manganese additions on the degradation and biocompatibility of magnesium-zinc-based alloys: In vitro and in vivo studies, *J. Magnesium Alloys*, 12(2024), No.2, p. 608.

[24] J. Li, Y. Zhang, M. Li, Y. Hu, Q. Zeng, and P. Zhang, Effect of combined addition of Zr, Ti and Y on microstructure and tensile properties of an Al-Zn-Mg-Cu alloy, *Materials & Design*, 223(2022), p. 111129.

[25] M. Qi, L. Wei, Y. Xu, J. Wang, A. Liu, B. Hao, and J. Wang, Effect of trace yttrium on the microstructure, mechanical property and corrosion behavior of homogenized Mg—2Zn—0.1Mn—0.3Ca—xY biological magnesium alloy, *Int. J. Miner. Metall. Mater.*, 29(2022), No.9, p. 1746.

[26] S. Jin, D. Zhang, X. Lu, Y. Zhang, L. Tan, Y. Liu, and Q. Wang, Mechanical properties, biodegradability and cytocompatibility of biodegradable Mg-Zn-Zr-Nd/Y alloys, *J. Mater. Sci. Technol.*, 47(2020), p. 190.

[27] F. Li, P. Guo, S. Han, C. Xu, J. Zhang, L. Yang, Z. Song, Y. Sun, W. Zhang, Q. Jia, and J. Kuan, A novel magnesium alloy with enhanced mechanical property,

degradation behavior and cytocompatibility, *Mater. Lett.*, 244(2019), p. 70.

[28] H. Jafari, A.H.M. Tehrani, M. Tehrani, and M. Heydari, Effect of extrusion process on microstructure and mechanical and corrosion properties of biodegradable Mg-5Zn-1.5Y magnesium alloy, *Int. J. Miner. Metall. Mater.*, 29(2022), No.3, p. 490.

[29] M.M. Zerankeshi, R. Alizadeh, E. Gerashi, M. Asadollahi, and T.G. Langdon, Effects of heat treatment on the corrosion behavior and mechanical properties of biodegradable Mg alloys, *J. Magnesium Alloys*, 10(2022), No.7, p. 1737.

[30] J. Chen, L. Tan, X. Yu, and K. Yang, Effect of minor content of Gd on the mechanical and degradable properties of as-cast Mg-2Zn-xGd-0.5Zr alloys, *J. Mater. Sci. Technol.*, 35(2019), No.4, p. 503.

[31] Z. Shi, and A. Atrens, An innovative specimen configuration for the study of Mg corrosion, *Corrosion Sci.*, 53(2011), No.1, p. 226.

[32] L.S. Bollen, New trends in biological evaluation of medical devices, *Medical device technology*, 16(2005), No.5, p. 10.

[33] J. Wang, F. Witte, T. Xi, Y. Zheng, K. Yang, Y. Yang, D. Zhao, J. Meng, Y. Li, W. Li, K. Chan, and L. Qin, Recommendation for modifying current cytotoxicity testing standards for biodegradable magnesium-based materials, *Acta Biomater.*, 21(2015), p. 237.

[34] E.E. Golub, G. Harrison, A.G. Taylor, S. Camper, and I.M. Shapiro, The role of alkaline phosphatase in cartilage mineralization, *Bone and mineral*, 17(1992), No.2, p. 273.

[35] E. Zhang, W. He, H. Du, and K. Yang, Microstructure, mechanical properties and corrosion properties of Mg-Zn-Y alloys with low Zn content, *Materials Science and Engineering a-Structural Materials Properties Microstructure and Processing*, 488(2008), No.1-2, p. 102.

[36] E.J.F. Dickinson, and A.J. Wain, The Butler-Volmer equation in electrochemical theory: Origins, value, and practical application, *J. Electroanal. Chem.*, 872(2020), p. 114145.

[37] B.J. Wang, D.K. Xu, S.D. Wang, L.Y. Sheng, R.-C. Zeng, and E.-h. Han, Influence of solution treatment on the corrosion fatigue behavior of an as forged Mg-Zn-Y-Zr alloy, *Int. J. Fatigue*, 120(2019), p. 46.

[38] L. Bao, Z. Zhang, Q. Le, S. Zhang, and J. Cui, Corrosion behavior and mechanism of Mg-Y-Zn-Zr alloys with various Y/Zn mole ratios, *J. Alloys Compd.*, 712(2017), p. 15.

[39] D. Kwon, H.V. Pham, P. Song, and S. Moon, Corrosion Behavior of the AZ31 Mg Alloy in Neutral Aqueous Solutions Containing Various Anions, *Metals*, 13(2023), No.5, p. 13050962.

[40] L.A. de Oliveira, R.M. Pereira da Silva, A.C. Dorion Rodas, R.M. Souto, and R.A. Antunes, Surface chemistry, film morphology, local electrochemical behavior and cytotoxic response of anodized AZ31B magnesium alloy, *J. Mater. Res. Technol-JMRT*, 9(2020), No.6, p. 14754.

[41] N.O. Laschuk, E.B. Easton, and O.V. Zenkina, Reducing the resistance for the use of electrochemical impedance spectroscopy analysis in materials chemistry, *RSC Adv.*, 11(2021), No.45, p. 27925.

[42] G. Uppal, A. Thakur, A. Chauhan, and S. Bala, Magnesium based implants for functional bone tissue regeneration - A review, *J. Magnesium Alloys*, 10(2022), No.2, p. 356.

[43] F. Cao, Z. Shi, J. Hofstetter, P.J. Uggowitzer, G. Song, M. Liu, and A. Atrens, Corrosion of ultra-high-purity Mg in 3.5% NaCl solution saturated with Mg(OH)2, *Corrosion Sci.*, 75(2013), p. 78.

[44] N.I.Z. Abidin, A.D. Atrens, D. Martin, and A. Atrens, Corrosion of high purity Mg, Mg2Zn0.2Mn, ZE41 and AZ91 in Hank's solution at 37 °C, *Corrosion Sci.*, 53(2011), No.11, p. 3542.

[45] Y. Xin, C. Liu, X. Zhang, G. Tang, X. Tian, and P.K. Chu, Corrosion behavior of biomedical AZ91 magnesium alloy in simulated body fluids, *Int. J. Mater. Res.*, 22(2007), No.7, p. 2004.

[46] A. Fijolek, J. Lelito, H. Krawiec, J. Ryba, and L. Rogal, Corrosion Resistance of Mg72Zn24Ca4 and Zn87Mg9Ca4 Alloys for Application in Medicine, *Materials*, 13(2020), No.16, p. 13163515.

[47] M.-j. Liang, C. Wu, Y. Ma, J. Wang, M. Dong, B. Dong, H.-h. Liao, J. Fan, and Z. Guo, Influences of aggressive ions in human plasma on the corrosion behavior of AZ80 magnesium alloy, *Materials Science & Engineering C-Materials for Biological Applications*, 119(2021), p. 111521.

[48] Y. Xin, K. Huo, T. Hu, G. Tang, and P.K. Chu, Corrosion products on biomedical magnesium alloy soaked in simulated body fluids, *Int. J. Mater. Res.*, 24(2009), No.8, p. 2711.

[49] A. Witecka, A. Bogucka, A. Yamamoto, K. Mathis, T. Krajnak, J. Jaroszewicz, and W. Swieszkowski, In vitro degradation of ZM21 magnesium alloy in simulated body fluids, *Materials Science & Engineering C-Materials for Biological Applications*, 65(2016), p. 59.

[50] B. Chen, K.-Y. Yin, T.-F. Lu, B.-Y. Sun, Q. Dong, J.-X. Zheng, C. Lu, and Z.-C. Li, AZ91 Magnesium Alloy/Porous Hydroxyapatite Composite for Potential Application in Bone Repair, *J. Mater. Sci. Technol.*, 32(2016), No.9, p. 858.

[51] J. Zhang, X. Ding, R. Chen, and J. Zhang, Corrosion behaviors of hot-extruded Mg96Y2Zn2 alloy in transverse and longitudinal directions: Guidance for parameters selection, *J. Alloys Compd.*, 923(2022), p. 166405.

[52] D.K. Xu, L. Liu, Y.B. Xu, and E.H. Han, The fatigue behavior of I-phase containing as-cast Mg-Zn-Y-Zr alloy, *Acta Mater.*, 56(2008), No.5, p. 985.

[53] Y. Song, D. Shan, R. Chen, and E.-H. Han, Effect of second phases on the corrosion behaviour of wrought Mg-Zn-Y-Zr alloy, *Corrosion Sci.*, 52(2010), No.5, p. 1830.

[54] D.K. Xu, W.N. Tang, L. Liu, Y.B. Xu, and E.H. Han, Effect of W-phase on the mechanical properties of as-cast Mg-Zn-Y-Zr alloys, *J. Alloys Compd.*,

461(2008), No.1-2, p. 248.

[55] W. Wang, H. Wu, R. Zan, Y. Sun, C. Blawert, S. Zhang, J. Ni, M.L. Zheludkevich, and X. Zhang, Microstructure controls the corrosion behavior of a lean biodegradable Mg-2Zn alloy, *Acta Biomater.*, 107(2020), p. 349.

[56] X. Gai, C. Liu, G. Wang, Y. Qin, C. Fan, J. Liu, and Y. Shi, A novel method for evaluating the dynamic biocompatibility of degradable biomaterials based on real-time cell analysis, *Regener. Biomater.*, 7(2020), No.3, p. 321.

[57] Z. Zhao, G. Li, H. Ruan, K. Chen, Z. Cai, G. Lu, R. Li, L. Deng, M. Cai, and W. Cui, Capturing Magnesium Ions via Microfluidic Hydrogel Microspheres for Promoting Cancellous Bone Regeneration, *Acs Nano*, 15(2021), No.8, p. 13041.

[58] P. Li, C. Schille, E. Schweize, E. Kimmerle-Mueller, F. Rupp, A. Heiss, C. Legner, U.E. Klotz, J. Geis-Gerstorfer, and L. Scheideler, Selection of extraction medium influences cytotoxicity of zinc and its alloys, *Acta Biomater.*, 98(2019), p. 235.

[59] ISO10993-12, Biological Evaluation of Medical Devices—Part 5: Tests for In Vitro Cytotoxicity. Geneva, Switzerland: International Organization for Standardization, 2009.

[60] Y. Kang, B. Du, Y. Li, B. Wang, L. Sheng, L. Shao, Y. Zheng, and T. Xi, Optimizing mechanical property and cytocompatibility of the biodegradable Mg-Zn-Y-Nd alloy by hot extrusion and heat treatment, *J. Mater. Sci. Technol.*, 35(2019), No.1, p. 6.

[61] I. Johnson, D. Perchy, and H. Liu, In vitro evaluation of the surface effects on magnesium-yttrium alloy degradation and mesenchymal stem cell adhesion, *J. Biomed. Mater. Res. Part A*, 100A(2012), No.2, p. 477.

[62] S. Yasuura, T. Ueno, S. Watanabe, M. Hirose, and T. Namihisa, Immunocytochemical localization of myosin in normal and phalloidin-treated rat hepatocytes, *Gastroenterology*, 97(1989), No.4, p. 982.